Commun. Comput. Phys.
doi: 10.4208/cicp.110315.190815a

Vol. **19**, No. 4, pp. 998-1014
April 2016

Simulation of Flow in Multi-Scale Porous Media Using the Lattice Boltzmann Method on Quadtree Grids

Lei Zhang[1,2], Qinjun Kang[2,*], Li Chen[3,2] and Jun Yao[1,*]

[1] *School of Petroleum Engineering, China University of Petroleum, Qingdao, Shandong 266580, China.*
[2] *Computational Earth Science Group (EES-16), Earth and Environmental Sciences Division, Los Alamos National Laboratory, Los Alamos, NM 87545, USA.*
[3] *Key Laboratory of Thermo-Fluid Science and Engineering of MOE, School of Energy and Power Engineering, Xi'an Jiaotong University, Xi'an, Shaanxi 710049, China.*

Communicated by Lianjie Huang

Received 11 March 2015; Accepted (in revised version) 19 August 2015

Abstract. The unified lattice Boltzmann model is extended to the quadtree grids for simulation of fluid flow through porous media. The unified lattice Boltzmann model is capable of simulating flow in porous media at various scales or in systems where multiple length scales coexist. The quadtree grid is able to provide a high-resolution approximation to complex geometries, with great flexibility to control local grid density. The combination of the unified lattice Boltzmann model and the quadtree grids results in an efficient numerical model for calculating permeability of multi-scale porous media. The model is used for permeability calculation for three systems, including a fractured system used in a previous study, a Voronoi tessellation system, and a computationally-generated pore structure of fractured shale. The results are compared with those obtained using the conventional lattice Boltzmann model or the unified lattice Boltzmann model on rectangular or uniform square grid. It is shown that the proposed model is an accurate and efficient tool for flow simulation in multi-scale porous media. In addition, for the fractured shale, the contribution of flow in matrix and fractures to the overall permeability of the fractured shale is studied systematically.

AMS subject classifications: 76S05, 76D05, 65Y10

Key words: Quadtree grid, unified lattice Boltzmann method, permeability, fractured porous media.

*Corresponding author. *Email addresses:* zhlei84@163.com (L. Zhang), qkang@lanl.gov (Q. Kang), lichenmt@lanl.gov (L. Chen), yaojunhdpu@126.com (J. Yao)

 ©2016 Global-Science Press

https://doi.org/10.4208/cicp.110315.190815a Published online by Cambridge University Press

1 Introduction

Flow in porous media usually occurs across multiple length scales. One example is gas flow in shale. The pore size of shale ranges from nanometers to micrometers, and the size of natural and hydraulic fractures varies from microns to centimeters, even meters. Therefore, multi-scale models are needed both to capture flow details in the finest length scale, and to handle the large scale of practical interest. The lattice Boltzmann method (LBM) [1], with a mesoscopic origin, is a promising numerical model for simulating flow in multiscale porous media. In recent years, the LBM has been successfully applied to a variety of fields, such as flows in porous media [2], chemical reactions [3, 4], heat transfer [5], particle suspensions [6], dissolution and precipitation [7–9], and multiphase and multicomponent flows [10, 11].

Because of its advantage in dealing with complex geometries/boundaries, the applications of the LBM to porous media have been mainly focused on the pore scale, with individual pores/grains fully resolved. However, some efforts have been devoted to extending it to flow simulation at the REV (representative elementary volume) scale. The basic idea is to introduce a resistance force to alter the local flow velocity, which was adopted in early work on lattice gas automata [12]. Spaid and Phelan [13] proposed a model based on the Brinkman equation for single-component flow in porous media. Later, Freed [14]extended the above model, rendering it to recover flow through a resistance field with arbitrary values of the resistance tensor components. In the model, the usual computational nodes were replaced with porous media nodes in the volume supposed to be occupied by a porous medium. However, due to the linear velocity dependence of the dimensionless resistance, the influence of Mach number is qualitatively different than that due to true inertial effects. Guo and Zhao [15] proposed a model for isothermal incompressible flow in porous media with linear and nonlinear matrix drag components as well as the inertial and viscous forces taken into account, by introducing the porosity into the equilibrium distribution and adding a force term to the evolution equation. By extending Freed's model into nonuniform grids, Kang *et al.* [16] developed a unified lattice Boltzmann model (ULBM) applicable to systems of various length scales, as well as to systems where multiple length scales coexist. The length of the scales can be as small as pore scales (on the order of microns), as large as field scales (on the order of meters to kilometers), or a mixture of various scales. The ULBM can recover Brinkman's equation or Darcy's equation under different situations. The ULBM treats the porous medium nodes, pore nodes, and wall nodes in the same way, even though they are at different length scales. There are no internal boundaries in the simulation. However, because the nonuniform meshes used in their model are rectangular, the applications of the ULBM have been very limited. For example, in simulation of flow through a fractured system, the fracture has to have smooth surface and has to be in parallel with the coordinates.

Therefore, to expand the applications of the ULBM, it is necessary to extend it to more general meshes. In fact, to increase numerical efficiency, several efforts have been made

https://doi.org/10.4208/cicp.110315.190815a Published online by Cambridge University Press

to treat the curved boundaries and to control the grid density at desirable regions in the conventional LBM [17–25], including development of LBM on quadtree grids [26,27]. Quadtree grids, as a particular type of unstructured grid, consist of congruent square cells of different sizes, which are constructed by recursive subdivision from an initial square domain according to prescribed yet flexible criteria [28,29]. Quadtree grids have gained increasing popularity in recent years due to many of their obvious advantages: mesh generation is automatic; mesh information is stored in simple hierarchical data structures; and locally high-resolution, dynamically adaptive grid is easy to achieve. Crouse *et al.* [30] adopted quadtree grids in the LB method. Because the linear interpolation [18] was used in the interface treatment, the second-order accuracy of the LBM could not be maintained. Chen *et al.* [26,27] also adopted the linear interpolation [17] in the quadtree grids, but used a back-and-forth error compensation and correction (BEFECC) method to achieve the second-order accuracy [31–33].

In this paper, the ULBM [16] is extended to quadtree grids [26,27] to solve fluid flow in some multi-scale porous media. The rest of the paper is organized as follows: In Section 2, the quadtree grid generation method, the ULBM, as well as the ULBM on quadtree grids are introduced; In Section 3, three simulation examples are presented; and in Section 4, some conclusions are drawn.

2 Mathematical model and numerical method

2.1 Quadtree grid

The primary units of quadtree grids are quadtree cells. Each quadtree cell is composed of four grid nodes. There are two different types of quadtree cells, the parent and leaf cells. A parent cell has four children and is equally divided into four subcells. A leaf cell has no children.

A scale function is often used to control grid density, which determines the length of each cell. When the length of a cell is greater than its associated scale function, the cell will be divided. The division goes on recursively until the cell length is smaller than its associated scale function. As an example, we construct a nonuniform quadtree grid on a 1×1 square domain based on the predefined scale function as shown in Fig. 1. The procedure can be summarized as follows:

Step 1. Define the scale function for the unit cell.

Step 2. Compare the scale function with the length of the cell; divide the cell into four cells if the scale function is less than the length of the cell.

Step 3. Repeat step 2 until the length of each cell is smaller than its corresponding scale function.

From the above procedure it is clear that the scale function can control the grid density. The area that needs coarse grid should be given a greater scale function value than

https://doi.org/10.4208/cicp.110315.190815a Published online by Cambridge University Press

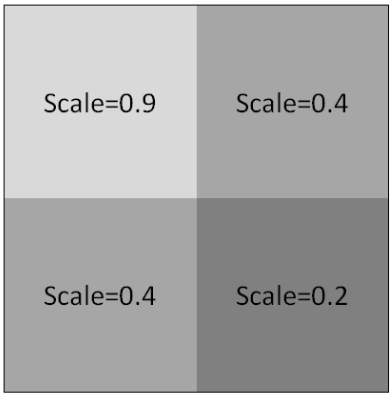


Figure 1: A unit square domain with a scale function distribution.

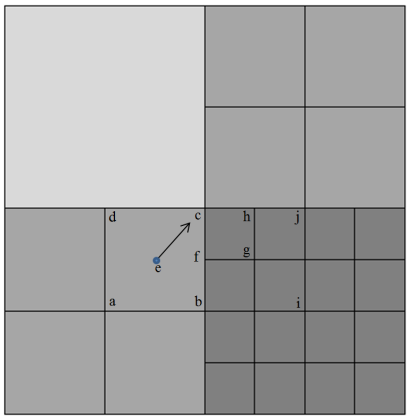


Figure 2: The quadtree grid of the unit square. Both cell abcd and cell fghc are leaf cells. Cell bijc is a parent cell containing four subcells.

the area that needs fine grid. For example, in a fractured system, the fracture needs finer grid than the matrix. Then the value of the scale function in the matrix should be set at a larger value than that in the fracture. Also the scale function should be set such that in the final grid, no cell has a side length more than twice the size of its neighbors. This simplifies the interpolation and ensures smooth transition of the macroscopic variables across the interface between cells of different levels [34, 35].

The quadtree grid generation described above is fast, automatic, robust and straightforward in concept. Fig. 2 illustrates the final grid of the unit square domain, where both cell abcd and cell fghc are leaf cells, while cell bijc is a parent cell, containing four subcells. If the flow domain is not square, one can simply cover the flow domain with a square and delete the grid nodes outside of the flow domain.

https://doi.org/10.4208/cicp.110315.190815a Published online by Cambridge University Press

2.2 Unified lattice Boltzmann method

Here we give a brief review of the unified LB model. More details can be found in [16]. It has been known that the LBM evolution equation, with a single relaxation time, i.e., the so-called lattice Bhatnagar-Gross-Krook (LBGK) model [36], is as follows:

$$f_i(\mathbf{x}+\mathbf{e}_i\delta_t,t+\delta_t)=f_i(\mathbf{x},t)-\frac{f_i(\mathbf{x},t)-f_i^{eq}(\rho,\mathbf{u},T)}{\tau}, \tag{2.1}$$

where f_i is the particle velocity distribution function on the i direction, δ_i is the time step, τ is relaxation time relating to the kinematic viscosity by $v=(\tau-0.5)RT$, and f_i^{eq} is the equilibrium distribution function, which is given by:

$$f_i^{eq}(\rho,\mathbf{u},T)=\omega_i\rho\left[1+\frac{\mathbf{e}_i\cdot\mathbf{u}}{RT}+\frac{(\mathbf{e}_i\cdot\mathbf{u})^2}{2(RT)^2}-\frac{\mathbf{u}^2}{2RT}\right], \tag{2.2}$$

where R is the gas constant, and $\mathbf{u}$, ρ and T are the velocity, density and temperature of the fluid, respectively. For the D2Q9 model, the weight coefficients are $\omega_0=4/9$, $\omega_i=1/9$ for $i=1,2,3,4$, and $\omega_i=1/36$ for $i=5,6,7,8$. The lattice velocities $\mathbf{e}_i$ are defined as $\mathbf{e}_0=(0,0)$, $\mathbf{e}_{1,3}=(\pm1,0)$, $\mathbf{e}_{2,4}=(0,\pm1)$, $\mathbf{e}_{5,7}=(\pm1,\pm1)$ and $\mathbf{e}_{6,8}=(\mp1,\pm1)$. The density and velocity of the fluid are calculated using $\rho=\sum_i f_i$ and $\rho\mathbf{u}=\sum_i \mathbf{e}_i f_i$.

For the ULBM, two more velocities are introduced [16]: $\mathbf{u}'$ and $\overline{\mathbf{u}}$, which are based on the fluid velocity $\mathbf{u}$ and given by:

$$\mathbf{u}'=\left[\underline{\underline{I}}+\frac{1}{2}\underline{\underline{R}}\right]^{-1}\left[\underline{\underline{I}}-\left(\tau-\frac{1}{2}\right)\underline{\underline{R}}\right]\cdot\mathbf{u}, \tag{2.3}$$

$$\overline{\mathbf{u}}=\left(1-\frac{1}{2\tau}\right)\mathbf{u}+\frac{1}{2\tau}\mathbf{u}. \tag{2.4}$$

$\underline{\underline{R}}$ is the resistance tensor, which depends on the permeability tensor $\underline{\underline{k}}$, and is defined as $\underline{\underline{R}}=v\underline{\underline{k}}^{-1}$. When the resistance tensor is diagonal, Eq. (2.3) can be written as

$$u_\alpha{}'=\frac{1-\left(\tau-\frac{1}{2}\right)R_a}{1+\frac{1}{2}R_a}u_\alpha. \tag{2.5}$$

Then the equilibrium distribution function is modified as follows:

$$f_i^{eq}(\rho,\mathbf{u},T)=\omega_i\rho\left[1+\frac{\mathbf{e}_i\cdot\mathbf{u}'}{RT}+\frac{(\mathbf{e}_i\cdot\overline{\mathbf{u}})^2}{2(RT)^2}-\frac{\overline{\mathbf{u}}^2}{2RT}\right]. \tag{2.6}$$

According the Chapman-Enskog expansion, Eq. (2.1) recovers the following macroscopic transport equations [16]:

$$\frac{\partial\rho}{\partial t}+\nabla\cdot(\rho\mathbf{u})=0, \tag{2.7}$$

$$\frac{\partial(\rho\mathbf{u})}{\partial t}+\nabla\cdot(\rho\mathbf{u}\mathbf{u})=-\nabla p-\rho\underline{\underline{R}}\cdot\mathbf{u}+\nabla\cdot[\rho v(\nabla\mathbf{u}+\mathbf{u}\nabla)]. \tag{2.8}$$

https://doi.org/10.4208/cicp.110315.190815a Published online by Cambridge University Press

We can see that Eq. (2.8) recovers Brinkman's equation when the inertial terms on the left-hand side can be neglected. The last term in this equation is called the Brinkman correction, which is usually much smaller than the linear velocity term for flow in porous media. Besides, at sites where permeability is very large, i.e., the resistance is very small, the linear velocity term is negligible compared to other terms and Eq. (2.8) recovers the Navier-Stokes equation.

2.3 Unified lattice Boltzmann method on quadtree grids

The way to implement the ULBM and the conventional LBM on quadtree grids is similar, because the calculations of Eqs. (2.3), (2.4), and (2.6) are all done at each grid point. Interpolation is needed only in the streaming step due to the data structure of the quadtree grids. For example, in a streaming step, node c (Fig. 2) will get information from nodes f, g, h, as well as point e, which is not a grid node. Due to the data structure, it is convenient and efficient to obtain e's information by linear interpolation of nodes a and c, which are in the same quadtree cell. However, this will normally lead to first-order accuracy only. In order to maintain the second-order accuracy of the LBM, Chen *et al.* [26,27] adopted the back-and-forth error compensation and correction (BFECC) method, which is also adopted in the present study. The details of implementing BFECC can be found in [26,27] and won't be repeated here.

The ULBM on quadtree grids retains all the advantages of the conventional LBM, such as ease of programming, the capability to incorporate microscopic interactions, and the inherent parallelism, except that in the case of parallel computation, additional attention should be paid to ensure load balance due to the unstructured nature of the quadtree grids.

3 Numerical examples

3.1 Fractured system

The fractured system used in Ref. [16] is adopted here to verify the ULBM with quadtree grids. The fractured system, shown in Fig. 3, is constructed by mirroring the original porous medium and leaving a fracture between the original medium and its image. The size of the fractured system is 255×530, and the width of fracture is 20, both in lattice units. With the unified model, there is no detailed geometry in the porous media. The original porous medium and its mirror are considered as a homogeneous porous medium. And each node in the porous media has the same permeability 0.59 (lattice units), which is used as input in the current model.

In the simulation, the left side is the entrance and the right side is the exit. The pressure (density) boundary condition [37] is adopted on both ends, and periodic boundary condition is applied to the other two boundaries. The pressure drop (Δp) between the entrance and the exit is 0.05. In the conventional LB model, a uniform square grid is applied

https://doi.org/10.4208/cicp.110315.190815a Published online by Cambridge University Press

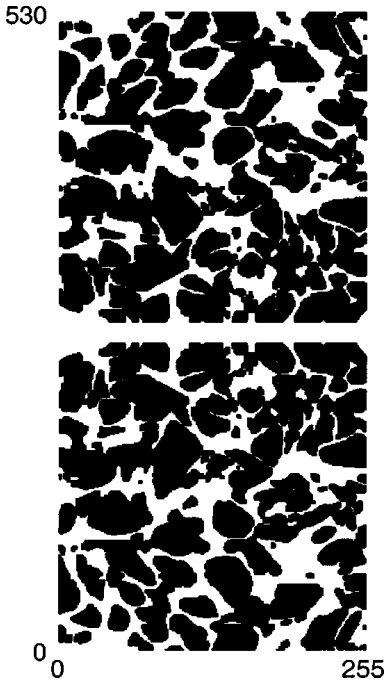


Figure 3: The fractured system used in Ref. [16].

to the system, and the mesh size is 256×531. In Ref. [16], a nonuniform grid was adopted and the mesh size was only 51×101. In this study, we generate the quadtree grid with three grid levels, as shown in Fig. 4. The level 1 grid is the coarsest grid and is used in the porous media, because the porous media are simplified as homogeneous media. Its scale function value is set to 4.5, so the grid spacing is 4. The level 3 grid is the finest grid that locates within the fracture, and its scale function value is set to 1.5, making the grid spacing 1. The level 2 grid locates between the finest grid and coarsest grid with a scale function value of 2.5, leading to a grid spacing of 2, which can ensure smooth transition of the macroscopic variables across the interface of different grid levels [34,35]. The total number of quadtree grid points is 19441. The relaxation time is set to 1.0 for both the quadtree grid and nonuniform grid. All the simulations in this study were performed on a single node of an Appro Xtreme-X cluster with dual-socket AMD 12-core MagnyCours processors. Each node has two 12-Core *AMD Opteron model 6176* processors and 64 GB DDR3 memory. The CPU runs at 2.3 GHz.

The permeability in a region is calculated by [16]

$$k=\frac{\overline{u}\mu l}{\Delta p}, \tag{3.1}$$

where $\overline{u}$ is the average horizontal velocity in this region, μ is the fluid viscosity, Δp is the pressure drop between the entrance and the exit, and l is the region length. Table 1 shows

https://doi.org/10.4208/cicp.110315.190815a Published online by Cambridge University Press

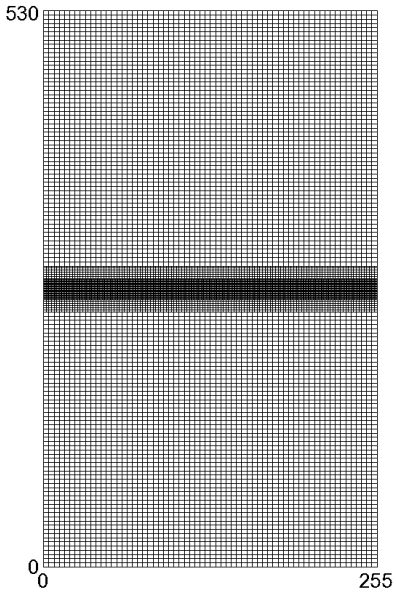


Figure 4: Quadtree grid for the fractured system shown in Fig. 3.

Table 1: Predicted permeability values for the fractured system used in Ref. [16].

	Top half	Bottom half	Fracture	Overall
Uniform grid	0.64	0.64	35.31	1.94
Nonuniform grid [16]	0.61	0.61	37.01	1.99
Quadtree grid	0.68	0.67	33.80	1.88

the permeability of the top half, the bottom half, the fracture and the entire fractured system, obtained using uniform square grid with conventional LB model, nonuniform rectangular grid with the ULBM [16], and quadtree grid with the ULBM, respectively. We consider the permeability values predicted by the conventional LBM "true" values. It is clear that unlike the ULBM on nonuniform rectangular grid, which underpredicts the permeability of the porous media, but overpredicts that of the fracture, the ULBM on quadtree grid predicts the highest permeability value for the porous matrix, but the lowest value for the fracture. Because the fracture plays a dominant role in determining the permeability of the fractured system, consequently, the ULBM on nonuniform rectangular grid and on quadtree grid overpredicts and underpredicts the permeability of the entire fractured system, respectively. However, the relative error is less than 3.1% for both cases.

Although the nonuniform rectangular grid used in Ref. [16] has less total grid points than the quadtree grid in this study, it can only deal with simple situations where the fracture is a straight channel whose walls are parallel with the x-axis. The quadtree grid,

https://doi.org/10.4208/cicp.110315.190815a Published online by Cambridge University Press

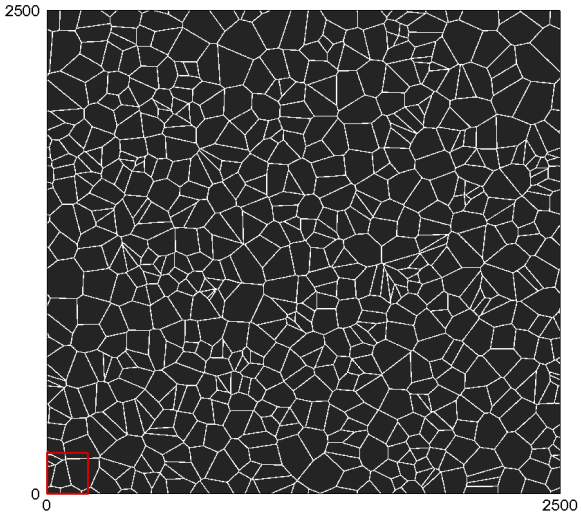


Figure 5: The Voronoi tessellation system.

however, can deal with much more complex fractured systems. This advantage cannot be demonstrated in this example, but can be seen in the next two simulation examples.

3.2 Voronoi tessellation

In this simulation example, the Voronoi tessellation shown in Fig. 5 is used. This pore geometry, provided by Prof. Xiaolong Yin from Colorado School of Mines, was generated using an algorithm based on Voronoi diagrams. The Voronoi diagram is a well-established computational geometry algorithm that, starting from a set of randomly distributed points (Poisson points), divides a two-dimensional or three-dimensional domain into many non-overlapping polygons (2D) or polyhedrons (3D) [38]. In two-dimensional Voronoi diagrams, the vertices of the polygons are always connected to three other vertices. Finally, the edges of polygons are given a finite width to form a network of channels, and the polygons represent the grains of the porous media. In this particular Voronoi tessellation, the width of the polygon edges are set to 6 lattices, and a total of 660 grains are contained. For more details, one can refer to Ref. [39]. In our simulation, the flow resistance of grains is set to infinity, and that in the channels is set to zero.

In our simulation, the size of the computational domain is 2500×2500. The width of the channel has a minimum value of 6, which is sufficient for permeability calculation [39]. The porosity of the entire system is 0.11. In the ULBM, the resistance of grains to flow is set to infinity, leading to no-slip condition at the fluid-solid interfaces, and the resistance in the channel is set to zero. The boundary condition is the same as that used in Section 3.1, so is the pressure drop. Similar to Section 3.1, a quadtree grid with three grid levels is used, with the coarsest level 1 grid (with a grid spacing of 4) in the polygons

https://doi.org/10.4208/cicp.110315.190815a Published online by Cambridge University Press

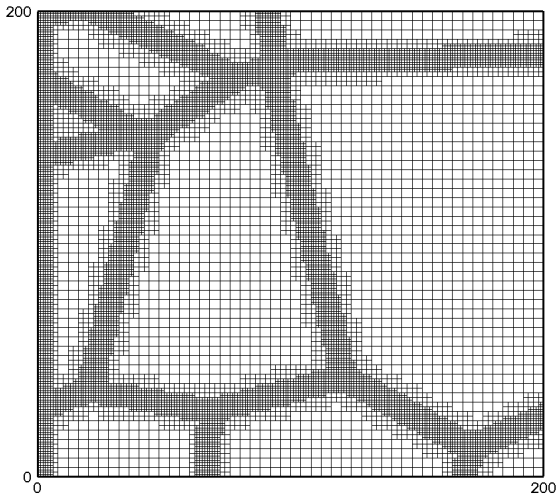


Figure 6: A part of quadtree grid of the Voronoi tessellation.

Table 2: Number of grid points, computational time and predicted permeability for the Voronoi tessellation.

	Number of grid points	Time per 1000 steps	Effective permeability
Uniform grid	6250000	1.6h	0.1554
Quadtree grid	2414885	0.7h	0.1536
Relative difference	61.4%	56.3%	1.2%

(grains), the finest level 3 grid (with a grid spacing of 1) within the channel, and the level 2 grid between the finest grid and coarsest grid. The grid of a 200×200 subdomain (bottom left corner of Fig. 5) is shown in Fig. 6.

In order to verify the result with the quadtree grid, a uniform square grid with the ULBM is also used to simulate flow through the Voronoi tessellation system. The results are shown in Table 2. The total number of grid points for the uniform square meshes is 6250000 (2500×2500). While the total number of grid points for the quadtree meshes is only 2414885, a decreases of about 61.4%. The permeability of the system is 0.1554 with the uniform square grid, and is 0.1536 with the quadtree grid. The relative error is less than 1.2%. The computational time using these two grids is quite different. It takes 1.6 hours for every 1000 steps for the uniform square grid, but only 0.7 hour for the quadtree grid due to fewer grids points.

Fig. 7 shows the density distribution and streamlines of flow through the Voronoi tessellation. The density decreases from the inlet to the outlet. Note that the grains and channel are initialized with equal fluid density at the same X coordinate. Fig. 7 also shows some streamlines of the Voronoi tessellation. The fluid only flows in the channel due to zero permeability of grains. There is no preferred flow pathway in the tessellation, because most of the channels have the same width.

https://doi.org/10.4208/cicp.110315.190815a Published online by Cambridge University Press

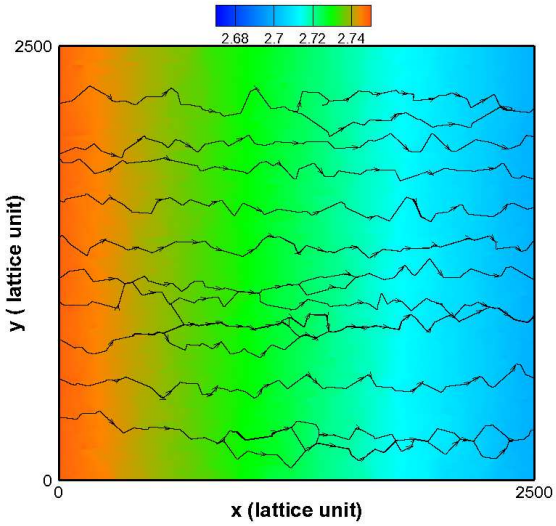


Figure 7: Streamlines and density distribution in the Voronoi tessellation.

3.3 Fractured shale

In this section, we apply our model to a computationally-generated pore structure of fractured shale. Initially developed in the 1940s, hydraulic fracturing is now a widely used technique to increase the permeability of a shale formation by extending and/or widening existing fractures and creating new ones through the injection of a pressurized fluid into shale reservoirs [40]. Due to natural and hydraulic fractures, both shale matrix and fracture system exist inside the shale reservoirs. Here we will calculate the permeability of the fractured shale and study the contribution of matrix and fractures to the overall permeability.

3.3.1 Physical model and quadtree grid

Three fractures are generated randomly in a domain of 1024×512, as shown in Fig. 8. The fractured system includes one major fracture in the middle and two branching fractures. The width of the major fracture is 10 lattices, and the width of the branching fractures is 8 lattices. The fracture volume fraction is 6.54%. Similar as in Sections 3.1 and 3.2, a quadtree grid with three grid levels is used. Fig. 9 shows part of the quadtree grid (250 to 350 in x direction and 200 to 300 in y direction). The scale function is set to 4.5, 2.5 and 1.5, same as in previous systems. The level 1 grid is used in the matrix, with a grid spacing of 4; the level 3 grid is used in the fractures, with a grid spacing of 1; and the level 2 grid locates between the finest grid and coarsest grid to ensure a smooth transition. The number of the total grid points is 116217, 22.2% of that of the uniform grid (1024×512).

The boundary condition is the same as that used in Sections 3.1 and 3.2. First, the matrix is set as impermeable and the resistance in the fractures is set to zero. The perme-

https://doi.org/10.4208/cicp.110315.190815a Published online by Cambridge University Press

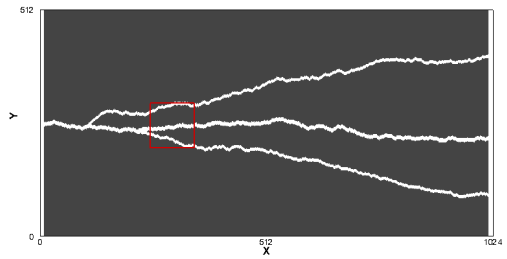


Figure 8: Schematic of a fractured shale formation.

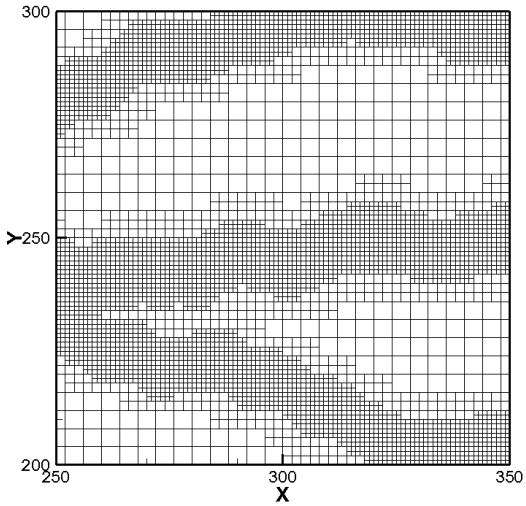


Figure 9: A part of the quadtree grid of the fractured shale shown in Fig. 8.

Table 3: Number of grid points, computational time and predicted permeability for the fractured shale.

	Number of grid points	Time per 1000 steps	Effective permeability
Uniform grid	524288	7.6 min	0.1978
Quadtree grid	116217	2 min	0.1942
Relative difference	77.8%	73.7%	1.82%

ability of the fractured system obtained using quadtree grid and uniform grid is 0.1978 and 0.1942, respectively. The relative error is less than 2%. These results are shown in Table 3.

3.3.2 Effect of matrix permeability

In this section, we investigate the contribution of the matrix to the permeability of the whole system. Here the fractures in Fig. 8 are considered as natural fractures in shale

https://doi.org/10.4208/cicp.110315.190815a Published online by Cambridge University Press

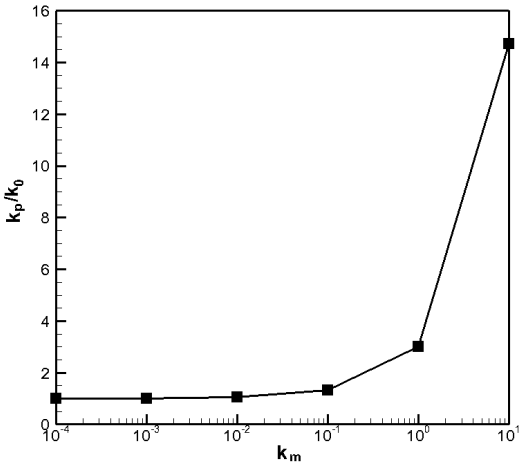


Figure 10: Dependency of k_p/k_0 on k_m, where k_m is the input permeability of matrix; k_p is the calculated permeability of whole system with different k_m; k_0 is the calculated permeability of whole system with impermeable matrix. The resistance in fracture is zero for all cases.

formations. We assume that 1 lattice represents 100 nm. The width of nature fracture is on the order of microns.

In the simulations, the permeability of matrix k_m is set to 10^{-4}, 10^{-3}, 10^{-2}, 10^{-1}, 10^{0} and 10^{1}, and the resistance in the fracture is set to zero. The permeability of whole system k_p is calculated using the ULBM with quadtree grid. Fig. 10 shows the dependence of k_p/k_0 on the matrix permeability k_m, where k_0 is permeability of the whole system with impermeable matrix and zero resistance in the fractures. As can be seen, k_p/k_0 is almost one when k_m is less than 10^{-1}, meaning that fluid flow in the matrix has no contribution to the whole system. To give it more physical meaning, we convert the permeability values to physical units. With the spatial resolution of 100nm, k_m of 10^{-1} in lattice unit corresponds to 10^{-15} m^2 ($10^{-1}\times10^{-7}\times10^{-7}$). The shale permeability varies from 10^{-17} to 10^{-22} m^2 [41] for various rock type, less than this critical permeability value (10^{-15} m^2). This indicates that for the fractured system shown in Fig. 8, flow in shale matrix has almost no contribution to the entire system, consistent with the common view on production mechanisms in shale that "gas can be produced only when extensive networks of natural fractures exist because the formations are so tight" [42]. Of course, for a system with a very different fracture volume fraction, the critical matrix permeability, might be very different [16].

3.3.3 Effect of resistance in fracture

In the simulations in Section 3.3.2, the resistance in the fractures is set to zero, meaning that the fractures are all open fractures. In hydraulic fracturing, proppants are often added into the fracturing liquid to prevent the fractures from closing. However, these proppants will also decrease the permeability of open fractures by blocking the flow. The

https://doi.org/10.4208/cicp.110315.190815a Published online by Cambridge University Press

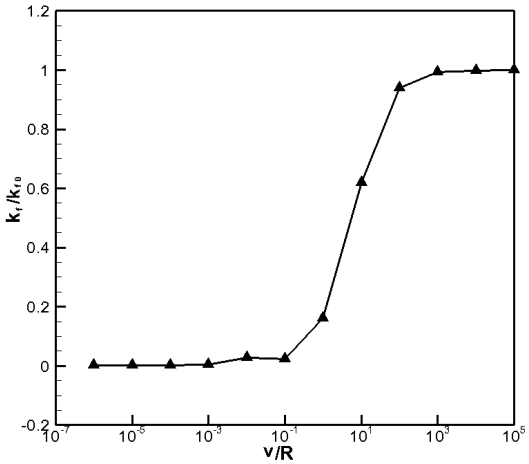


Figure 11: Dependency of k_f/k_{f0} on v/R, where v is the fluid viscosity; R is the resistance of fractures; k_f is the calculated permeability of the fracture shale; k_{f0} is the calculated permeability of fractured shale with infinite v/R. The matrix is impermeable for all cases.

decrease can be very different due to variable concentration and size of the proppants. In this study, the blocking effect is accounted for through the resistance R in the fractures, which is set such that k_R ($k_R = v/R$) varies from 10^{-6} to 10^5. Note k_R is different from the fracture permeability. Instead, its value is assigned to every node within the fracture, accounting for the flow blocking effect of proppants. This value is infinite (corresponding to zero resistance) in the absence of proppants. Fig. 11 gives the dependence of k_f/k_{f0} on v/R, where k_f is the calculated permeability of the fracture shale, and k_{f0} is the value of k_f when v/R is infinite, i.e., the resistance is zero. In these simulations, the permeability of the matrix is set to zero. We can see from Fig. 11 two points of particular interest, i.e., v/R equals 10^{-1} and 10^3. When v/R is less than 10^{-1}, the ratio of k_f/k_{f0} is almost zero. This corresponds to the case where the proppants almost completely block the fluid flow in the fracture. When v/R is greater than 10^3, the ratio of k_f/k_{f0} is almost unity. In this case, the flow blocking by proppants is negligible. The ratio of k_f/k_{f0} increases rapidly when v/R ranges from 10^{-1} to 10^3, indicating that the concentration and size of proppant have significant effect on the permeability of fracture in certain range.

4 Conclusions

We have combined the ULBM with quadtree grids to simulate flow in multiscale porous media. The ULBM treats the porous medium nodes, pore nodes, and wall nodes in the same way. The quadtree grids can be generated automatically and dynamically with desired local grid density based on certain criteria. The combined model has been applied to three porous media for permeability calculation. Simulations were first performed on

https://doi.org/10.4208/cicp.110315.190815a Published online by Cambridge University Press

a fractured system used in [16] and a Voronoi tessellation system, in order to validate the model. For both systems, three grid levels were used in the quadtree grids. For the fractured system, the results of the ULBM on quadtree grid were compared with those of the conventional LBM and those of the ULBM on nonuniform rectangular grid obtained in [16]. Good agreement was found for the total permeability of the entire system. For the Voronoi tessellation, a flow simulation using the ULBM on square grid was also performed, and the results were compared with those of the ULBM on quadtree grid. The relative error for the permeability is less than 1.2%. However, the ULBM on quadtree grid used 61.4% fewer grid nodes and 56.3% less computation time.

Finally, the model was used to simulate flow in a fractured shale formation. Three fractures were generated randomly in the system, and a three-level quadtree grid was adopted. With zero resistance in the fractures, the matrix permeability was varied to study its effect on the overall permeability, to investigate the contribution of matrix to the permeability of the shale with natural fractures. Conversely, with zero permeability in the matrix, the resistance in the fractures was varied to study its effect on the overall permeability, to investigate the effect of fracture resistance (e.g., caused by proppants) on the permeability of shale with hydraulic fractures. For the natural fracture shale, it was found that for typical shale rocks and for the fractured system considered in this study, flow in the shale matrix has almost no contribution to the permeability of the entire system. For the hydraulic fracture shale, the concentration and size of proppant have significant effect on the permeability of the fractured shale. The simulation examples demonstrated that the combination of the ULBM and quadtree grid offers an accurate and efficient tool for flow simulation in multi-scale porous media.

Acknowledgments

We would like to thank the support from the National Natural Science Foundation of China (No. 51234007, No. 51504276), China Postdoctoral Science Foundation (No. 2015M580621), Introducing Talents of Discipline to Universities (B08028), Los Alamos National Laboratory's LDRD Program and Institutional Computing Program, as well as UC Lab Fees Research Program. Lei Zhang would like to thank Chinese Scholarship Council for supporting the one-year visit in Los Alamos National Laboratory. We also thank Prof. X. Yin from Colorado School of Mines for providing the Voronoi tessellation used in the second simulation example.

References

[1] S. Y. Chen and G. D. Doolen, Lattice Boltzmann methode for fluid flows. Annu. Rev. Fluid. Mech., 30 (1998), 329-364.
[2] N. S. Martys and H. Chen, Simulation of multicomponent fluids in complex three-dimensional geometries by the lattice Boltzmann method. Phys. Rev. E, 53 (1996), 743.

https://doi.org/10.4208/cicp.110315.190815a Published online by Cambridge University Press

[3] L. Chen, Q. Kang, Y.-L. He, and W.-Q. Tao, Pore-scale simulation of coupled multiple physicochemical thermal processes in micro reactor using lattice Boltzmann method Int. J. Hydrogen Energy 37 (2012), 13943-13957.
[4] L. Chen, Y.-L. He, Q. Kang, and W.-Q. Tao, Coupled numerical approach combining finite volume and lattice Boltzmann methods for multi-scale multi-physicochemical processes. J. Comput. Phys., 255 (2013), 83-105.
[5] L. Biferale, P. Perlekar, M. Sbragaglia, and F. Toschi, Convection in multiphase fluid flows using lattice Boltzmann methods. Phys. Rev. Lett., 108 (2012), 104502.
[6] A. S. Joshi and Y. Sun, Multiphase lattice Boltzmann method for particle suspensions. Phys. Rev. E, 79 (2009), 066703.
[7] Q. Kang, D. Zhang, S. Chen, and X. He, Lattice Boltzmann simulation of chemical dissolution in porous media. Phys. Rev. E, 65 (2002), 036318.
[8] Q. J. Kang, D. X. Zhang and S. Y. Chen, Simulation of dissolution and precipitation in porous media. J. Geophys. Res. Solid Earth, 108 (2003), 2505.
[9] L. Chen, Q. Kang, B. A. Robinson, Y.-L. He, and W.-Q. Tao, Pore-scale modeling of multiphase reactive transport with phase transitions and dissolution-precipitation processes in closed systems. Phys. Rev. E, 87 (2013), 043306.
[10] L. Chen, H.-B. Luan, Y.-L. He, and W.-Q. Tao, Pore-scale flow and mass transport in gas diffusion layer of proton exchange membrane fuel cell with interdigitated flow fields. Int. J. Therm. Sci., 51 (2012), 132-144.
[11] Q. J. Kang, P. C. Lichtner and D. X. Zhang, Lattice Boltzmann pore-scale model for multicomponent reactive transport in porous media. J. Geophys. Res. Solid Earth, 111 (2006), B05203.
[12] K. Balasubramanian, F. Hayot and W. F. Saam, Darcy's law from lattice-gas hydrodynamics. Phys. Rev. A, 36 (1987), 2248-2253.
[13] M. A. Spaid and F. R. Phelan Jr, Lattice Boltzmann methods for modeling microscale flow in fibrous porous media. Phys. Fluids, 9 (1997), 2468-2474.
[14] D. M. Freed, Lattice-Boltzmann method for macroscopic porous media modeling. Int. J. Mod. Phys. C, 9(1998), 1491-1503.
[15] Z. Guo and T. S. Zhao, Lattice Boltzmann model for incompressible flows through porous media. Phys. Rev. E, 66 (2002), 036304.
[16] Q. Kang, D. Zhang and S. Chen, Unified lattice Boltzmann method for flow in multiscale porous media. Phys. Rev. E, 66 (2002), 056307.
[17] X. He, L.-S. Luo and M. Dembo, Some progress in lattice Boltzmann method. Part I. nonuniform mesh grids. J. Comput. Phys., 129 (1996), 357-363.
[18] O. Filippova and D. Hänel, Grid refinement for lattice-BGK models. J. Comput. Phys., 147 (1998), 219-228.
[19] D. Yu, R. Mei and W. Shyy, A multi-block lattice Boltzmann method for viscous fluid flows. Int. J. Numer. Methods Fluids, 39 (2002), 99-120.
[20] F. Nannelli and S. Succi, The lattice Boltzmann equation on irregular lattices. J. Stat. Phys., 68 (1992), 401-407.
[21] N. Cao, S. Chen, S. Jin, and D. Martínez, Physical symmetry and lattice symmetry in the lattice Boltzmann method. Phys. Rev. E, 55 (1997), R21-R24.
[22] S. Ubertini and S. Succi, Recent advances of lattice Boltzmann techniques on unstructured grids. Prog. Comput. Fluid. Dy., 5 (2005), 85-96.
[23] N. Rossi, S. Ubertini, G. Bella, and S. Succi, Unstructured lattice Boltzmann method in three dimensions. Int. J. Numer. Methods Fluids, 49 (2005), 619-633.

https://doi.org/10.4208/cicp.110315.190815a Published online by Cambridge University Press

[24] Y. Li, E. J. LeBoeuf and P. K. Basu, Least-squares finite-element scheme for the lattice Boltzmann method on an unstructured mesh. Phys. Rev. E, 72 (2005), 046711.
[25] H.-B. Luan, H. Xu, L. Chen, D.-L. Sun, Y.-L. He, and W.-Q. Tao, Evaluation of the coupling scheme of FVM and LBM for fluid flows around complex geometries. Int. J. Heat Mass Transfer, 54 (2011), 1975-1985.
[26] Y. Chen, Q. J. Kang, Q. D. Cai, and D. X. Zhang, Lattice Boltzmann method on quadtree grids. Phys. Rev. E, 83 (2011), 10.
[27] Y. Chen and Q. D. Cai, The lattice Boltzmann method based on quadtree mesh. Mod. Phys. Lett. B, 23 (2009), 289-292.
[28] A. Klinger and C. R. Dyer, Experiments on picture representation using regular decomposition. Computer Graphics and Image Processing, 5 (1976), 68-105.
[29] H. Samet, The quadtree and related hierarchical data structures. ACM Comput. Surv., 16 (1984), 187-260.
[30] B. Crouse, E. Rank, M. Krafczyk, and J. Tölke, A LB-based approach for adaptive flow simulations. Int. J. Mod. Phys. B 17 (2003), 109-112.
[31] T. F. Dupont and Y. Liu, Back and forth error compensation and correction methods for removing errors induced by uneven gradients of the level set function. J. Comput. Phys., 190 (2003), 311-324.
[32] T. F. Dupont and Y. Liu, Back and forth error compensation and correction methods for semi-Lagrangian schemes with application to level set interface computations. Math. Comput., (2007), 647-668.
[33] K. Byung Moon, Y. Liu, I. Llamas, and J. Rossignac, Advections with Significantly Reduced Dissipation and Diffusion. IEEE Trans. Vis. Comput. Graph., 13 (2007), 135-144.
[34] P. L. Baehmann, S. L. Wittchen, M. S. Shephard, K. R. Grice, and M. A. Yerry, Robust, geometrically based, automatic two-dimensional mesh generation. Int. J. Numer. Methods Eng., 24 (1987), 1043-1078.
[35] S. Popinet, Gerris: A tree-based adaptive solver for the incompressible Euler equations in complex geometries. J. Comput. Phys., 190 (2003), 572-600.
[36] Y. H. Qian, D. D. Humières and P. Lallemand, Lattice BGK Models for Navier-Stokes Equation. Europhys. Lett., 17 (1992), 479-484.
[37] Q. Zou and X. He, On pressure and velocity boundary conditions for the lattice Boltzmann BGK model. Phys. Fluids, 9 (1997), 1591-1598.
[38] G. Voronoi, Nouvelles applications des paramèteres continus à la théorie des formes quadratiques. J. Reine. Angew. Math., 134 (1908), 198-287.
[39] M. Wu, F. Xiao, R. M. Johnson-Paben, S. T. Retterer, X. Yin, and K. B. Neeves, Single- and two-phase flow in microfluidic porous media analogs based on Voronoi tessellation. Lab. Chip., 12 (2012), 253-261.
[40] A. Vengosh, R. B. Jackson, N. Warner, T. H. Darrah, and A. Kondash, A Critical Review of the Risks to Water Resources from Unconventional Shale Gas Development and Hydraulic Fracturing in the United States. Environ. Sci. Technol., 48 (2014), 8334-8348.
[41] M. Best and T. Katsube, Shale permeability and its significance in hydrocarbon exploration. The Leading Edge, 14 (1995), 165-170.
[42] E. S. Carlson and J. C. Mercer, Devonian shale gas production: Mechanisms and simple models. J. Petrol. Technol., 43 (1991), 476-482.

https://doi.org/10.4208/cicp.110315.190815a Published online by Cambridge University Press